

Analysis of Radio Frequency Interference Detection Algorithms in the Angular Domain for SMOS

Sidharth Misra, *Member, IEEE*, and Christopher S. Ruf, *Fellow, IEEE*

Abstract—Radio frequency interference (RFI) detection techniques have different challenges and opportunities for interferometric radiometers such as the Microwave Imaging Radiometer using Aperture Synthesis on the Soil Moisture and Ocean Salinity (SMOS) mission. SMOS does not have highly oversampled temporal resolution or subband filters for oversampled spectral resolution, as do other radiometers with enhanced RFI detection capabilities. It does, however, have multisampled angular resolution in the sense that a single location is viewed from many different angles of incidence. This paper compares and contrasts RFI detection algorithms that use measurements made at a variety of different levels of SMOS signal processing, including the visibility domain, brightness temperature spatial domain, and brightness temperature angular domain. The angular domain detection algorithm, in particular, is developed and characterized in detail. Examples of the algorithms applied to cases with RFI (to assess detection skill) and without RFI (to assess false-alarm behavior) are considered.

Index Terms—Interferometry, microwave radiometry, radio frequency interference (RFI), Soil Moisture and Ocean Salinity (SMOS).

I. INTRODUCTION

THE EUROPEAN Space Agency's Soil Moisture and Ocean Salinity (SMOS) mission [1], [2] has been steadily providing global maps of brightness temperature (T_b) since soon after its launch in November 2009. SMOS is responsible for retrieving measurements of sea-surface salinity and soil moisture at 1.4 GHz (the 21-cm hydrogen line) (or the L-band). Even though T_b measurements are made in a protected part of the spectrum, various airborne campaigns [3]–[5] have observed radio frequency interference (RFI) signals corrupting T_b measurements at the L-band. Initial SMOS measurements have also observed large amounts of RFI.

RFI is insidious in nature and, if left unmitigated, can result in erroneous estimates of geophysical parameters such as soil moisture [6]. Various RFI detection algorithms use techniques such as pulse detection in the temporal domain [7]–[9] or

spectrally divide the incoming signal into separate frequency bins [7], [10], [11]. Other detection algorithms operate in the statistical domain such as the kurtosis detection algorithm [12]–[14], where deviation of the incoming signal from normality is detected to identify RFI. Due to the unique nature of SMOS hardware, these conventional RFI detection techniques cannot be used for SMOS. SMOS measures T_b over a single 24-MHz passband centered at 1.413 GHz and thus cannot apply spectral subbanding RFI detection techniques. The temporal resolution of SMOS is not fine enough to apply a similar pulse-detection algorithm as is used by oversampled sensors [7]–[9].

Microwave Imaging Radiometer using Aperture Synthesis (MIRAS) is an interferometric radiometer used by SMOS for measuring T_b . Some RFI detection techniques specific to SMOS hardware have been developed, e.g., in [15], where unnatural third and fourth Stokes outliers are flagged as RFI sources. Another algorithm developed for SMOS detects point source RFI by applying a similar technique developed for SMOS to cancel Sun effects [16]. This paper presents an RFI detection algorithm that takes advantage of the unique signal processing properties of MIRAS. RFI mitigation and detection techniques can be applied at many different stages of the processing. This paper examines and compares the detectability of different RFI algorithms at the L1a stage (visibility domain), the spatial domain (T_b snapshot images), and the angular domain (T_b versus incidence angle).

In Section II, we give details of the various SMOS signal domains in which the RFI detection algorithm can be applied and present a new angular domain detection algorithm. A discussion of the differences in algorithm performance between domains is presented in Section III. Section IV presents representative results of the angular domain detection algorithm, before summarizing in Section V.

II. SMOS RFI DETECTION DOMAINS

The SMOS mission makes interferometric passive microwave measurements of the incoming thermal emission. The measurements are related to the Fourier transform of the spatial brightness temperature distribution and are referred to as visibility measurements. A 2-D “snapshot” T_b image is derived from the visibility domain by effectively taking an inverse Fourier transform of the visibility measurements. SMOS has an effective image field of view (FOV) of $1050 \times 650 \text{ km}^2$, and a snapshot is taken every 1.2 s [17]. This means that SMOS observes a single grid point on the Earth with multiple snapshots at different incidence angles.

Manuscript received April 11, 2011; revised August 17, 2011; accepted October 11, 2011. Date of publication December 28, 2011; date of current version April 18, 2012. This work was supported in part by the National Aeronautics and Space Administration (NASA) under the NASA Earth and Space Science Fellowship (NNX08AU76H).

S. Misra is with the Jet Propulsion Laboratory, Pasadena, CA 91109 USA (e-mail: sidharth.misra@jpl.nasa.gov).

C. S. Ruf is with the Department of Atmospheric, Oceanic and Space Sciences and the Space Physics Research Laboratory, University of Michigan, Ann Arbor, MI 48109 USA (e-mail: cruf@umich.edu).

Color versions of one or more of the figures in this paper are available online at <http://ieeexplore.ieee.org>.

Digital Object Identifier 10.1109/TGRS.2011.2176949

An RFI detection algorithm can, in principle, be applied at any phase of data processing. Errors introduced by RFI can propagate forward from correlation measurements to Level 2 soil moisture and salinity data products. Algorithms applied early in the processing pipeline can mitigate error propagation, but at a possible cost in detectability. Other algorithms, such as the one proposed in this paper, detect RFI after the SMOS L1b data but may have better detection performance. If RFI-free data products prior to L1b are of interest, then some other type of RFI detection and mitigation would be required.

The visibility, spatial, and angular domains are considered here for comparing RFI detection algorithms. Each domain is described hereinafter in greater detail.

A. Visibility Domain

The visibility domain is contained in the L1a data set produced by the SMOS program. This data set contains spatial frequency information about the Tb image. For example, the zeroth visibility measurement can be considered to be the dc component (or mean) of the image over the FOV, weighted by the antenna element pattern.

An RFI detection algorithm based in the visibility domain of SMOS has been developed which would operate on successive time-domain samples of the zeroth visibility data [18]. The zeroth visibility data are similar to data measured by a conventional (noninterferometric) radiometer, measuring the power of the incoming emissions. The algorithm is essentially a temporal RFI detection algorithm, wherein samples are compared to their neighboring (in time) pixels. Any outliers or spikes that deviate from the expected smooth variation by more than a preselected threshold are flagged as being corrupted by RFI.

Such an algorithm has the advantage of detecting RFI very early in the signal processing flow. Visibility measurements for SMOS have a relatively low NE Δ T noise level of approximately 0.2 K [19]. NE Δ T represents the radiometric uncertainty in the measurements. A low NE Δ T in the visibility measurement aids in RFI detection performance by reducing the false-alarm rate (FAR). Large RFI sources inside and outside the alias-free FOV [20] can be immediately identified by the aforementioned algorithm. Another advantage of RFI detection in this domain is the fact that the algorithm can utilize the positive definite L2-norm property of the zeroth visibility RFI perturbations [18]. That is, RFI is always positively biased. One limitation of RFI detection in the visibility domain is the fact that highly spatially localized sources (isolated hot spots) will have much lower signal amplitude in the visibility domain than in the spatial domain because the dc visibility samples are an average over the entire image, including regions without any RFI.

B. Spatial Domain

The next step in SMOS processing is to convert visibility measurements to Tb snapshots. This domain represents Tb values at individual grid point locations within the snapshot image FOV. A snapshot is taken every 1.2 s. Although obtaining Tb images from visibilities is slightly complex, it is based on a regularized inversion of the visibility measurement [26].

The resulting image contains aliased as well as alias-free Tb zones. The RFI detection algorithm operates in the alias-free FOV only.

Different versions of a spatial RFI detection algorithm have been applied in the past for microwave radiometer measurements (e.g., [21]). The basic principle of such algorithms is to compare the deviation of a pixel under test with its neighboring pixels in the spatial domain. The algorithm generally involves some sort of moving spatial averaging window. If the pixel under test deviates considerably from the mean with respect to some threshold, then the pixel is flagged as being corrupted. The spatial domain algorithm is effective at flagging isolated Tb spikes.

Compared to the visibility domain, the noise level is higher (with an NE Δ T of approximately 5 K) in the spatial domain due to error propagation through the inverse Fourier transform. This represents an increase in noise, relative to the visibility domain, by a factor of ~ 25 . The RFI power level will also increase as a result of the inverse Fourier transform. In this case, however, the increase will be by a factor of $\sim 25^2$ if the RFI source is spatially localized because the inverse Fourier transform will coherently focus the visibility measurements at the spot in the image where the RFI is located. This results in a higher signal-to-noise ratio (SNR), giving better detection performance. The main disadvantage of spatial detection algorithms is that natural geophysical variations within the spatial averaging window can cause RFI false alarms or missed detections. Also, due to the interferometric nature of the imaging, any strong RFI point sources suffer from the Gibbs phenomenon. That is, in the Tb snapshot image, a powerful RFI point source is surrounded by oscillating negative and positive annular rings. This results in RFI that can be negatively biased with respect to the mean neighbors. For this reason, spatial detection algorithms must be designed to detect both positively and negatively biased RFI pixels.

C. Angular Domain

SMOS has the unique advantage of observing a single grid point on the Earth over multiple incidence angles. As a result, an RFI detection algorithm can be applied in a domain that is one step further in the processing chain compared to the spatial domain. Detection of anomalous behavior in the Tb variation with respect to incidence angle is another method to aid in flagging RFI-corrupted measurements [22]. The angular domain algorithm is a primary focus of this paper.

Depending on the polarization being observed, Tb values tend to have a very specific dependence on incidence angle. This dependence is influenced by variables such as vegetation canopy, physical surface temperature, surface roughness, moisture content in the soil, salinity of water, etc. Knowledge of this relationship aids in the inversion of such geophysical variables such as soil moisture and sea-surface salinity. The principle behind this new type of RFI detection algorithm is that, if RFI is present in some but not all of the snapshots, a single geographic location that is contained in multiple images will exhibit outlier behavior due to RFI when Tb is viewed as a function of incidence angle.

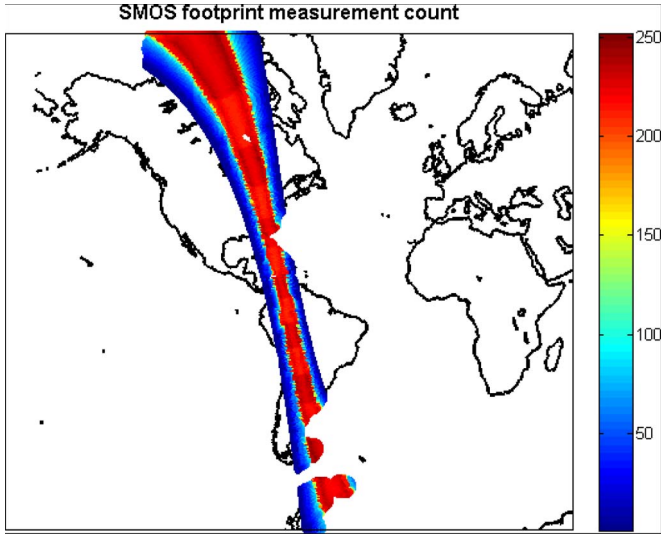


Fig. 1. SMOS semiorbit map indicating the number of multiple measurements made at a single grid location over various incidence angles.

RFI outliers detected in the angular domain have the same SNR that exists in the spatial domain. Detection in the angular domain takes advantage of the fact that there exists a much more deterministic relationship between the sample under test and its neighboring samples at other incidence angles, relative to the relationship between a spatial sample and its neighboring pixels. This allows for better prediction of an estimated value for the sample under test, based on the Tb values of its neighboring incidence angles at the same location, which results in a more accurate detection threshold. Another advantage of the angular domain detection algorithm is that, since the measurements are made at one grid point location, the detection statistics are not influenced by the spatial variability of neighboring pixels. One caveat with this method is that, over high incidence angles, the effective pixel footprint stretches and may be contaminated by neighboring spatial locations. In order to avoid such contamination, the angular domain algorithm operates only within a restricted range of incidence angles. As a result of such a restriction, any RFI present at incidence angles outside the operating range will go undetected by the angular domain algorithm. The angular domain algorithm is described in detail hereinafter.

1) *Algorithm Description:* The algorithm is used whenever there are a sufficient number of samples versus incidence angle at a grid point. The default number of samples required for the algorithm to operate is ten. As a result, most samples at the edge or “wing” of the SMOS hexagonal alias-free snapshot cannot have this RFI algorithm applied to it, whereas there are more samples near the center of the image. Fig. 1 indicates the number of multiple incidence angle measurements made at each grid location in the image over a half orbit. As expected, most of the counts are in the center of the swath, with lesser measurement points made at the edges.

The algorithm first collects all samples versus incidence angle at a grid point and flags any sample above 330 K or below 0 K as containing RFI. These samples are discarded from subsequent processing. If the number of remaining samples is more than six, then those samples are used to fit a third-order

polynomial to the dependence of Tb on incidence angle at that grid point.

In order to determine an RFI detection threshold, a cubic Tb relationship is estimated from the Tb measurements as given by

$$\hat{T}_i = c_0 + c_1\theta_i + c_2\theta_i^2 + c_3\theta_i^3 \quad (1)$$

where \hat{T}_i is the brightness temperature estimate at the i th incidence angle and θ_i and c_n ($n = 0, 1, 2, 3$) are the regression coefficients estimated from the measured Tb vector as shown below

$$C = \begin{bmatrix} c_0 \\ c_1 \\ c_2 \\ c_3 \end{bmatrix} = (\Theta'\Theta)^{-1}\Theta' \begin{bmatrix} T_1 \\ \vdots \\ T_m \end{bmatrix} \quad (2)$$

where

$$\Theta = \begin{bmatrix} 1 & \theta_1 & \theta_1^2 & \theta_1^3 \\ \vdots & \vdots & \vdots & \vdots \\ \vdots & \vdots & \vdots & \vdots \\ 1 & \theta_m & \theta_m^2 & \theta_m^3 \end{bmatrix}.$$

T_i are the measured Tb values at incidence angle θ_i .

The cubic fit is performed with all valid Tb measurement samples other than the sample under test. In this way, the fit is not impacted by any RFI corruption of the sample under test. Once the Tb estimate of the sample under test is obtained, detection is performed by comparing the absolute value of the difference between the estimated and the original Tb with some threshold, or

$$f_i = \begin{cases} 0 & \text{if } |\hat{T}_i - T_i| < 3S \\ 1 & \text{if } |\hat{T}_i - T_i| \geq 3S \end{cases} \quad (3)$$

where f is the RFI flag (0 means no RFI, and 1 means RFI) and $3S$ is the detection threshold. S is defined as the smaller of the measurement NE Δ T and the rms residual error in the cubic fit. If there is no RFI present in the Tb samples used to determine the cubic fit, its residual error tends to be smaller than the NE Δ T and the residual error is a more conservative detection threshold. If there are RFI-corrupted samples used in the cubic fit, then its residual error is greater and the NE Δ T is a better threshold.

In addition to the aforementioned threshold test, if a majority of the samples at a grid point are above 330 K and the number of samples necessary for a fit is insufficient, then all remaining samples are flagged as being corrupted by RFI. There is also a residual error metric with each flag that gives an indication of the confidence in the cubic fit and, hence, the trust in the detectability for that particular sample under test.

III. DOMAIN COMPARISON

SMOS can apply RFI detection algorithms at various stages of the processing tree. The three main domains considered here are visibility (L1a), spatial, and angular (L1c). There are advantages and disadvantages to applying RFI algorithms at these different stages. The following section discusses these.

A. Visibility Domain Versus Spatial Domain

Detection using the zeroth visibility will be compared to detection with a single Tb snapshot in the spatial domain. Comparisons will be based on two factors, the signal strength of RFI in the two domains and the noise increase going from one domain to another.

The zeroth visibility or the reference radiometer of MIRAS uses an antenna element with a real aperture. MIRAS as a whole synthesizes an effective aperture area that is larger than that of each individual element. Based on the Friis transmission formula [23], the power of an incoming RFI point source (P_r) is linearly proportional to the effective aperture of the receiver (A_r). MIRAS has a larger effective aperture (~ 7 m in diameter) than the reference radiometer (< 10 cm in radius), and hence, the signal strength of the RFI seen by the interferometer is stronger.

Another means of quantifying RFI signal strength is with respect to spatial resolutions. SMOS pixels have a spatial resolution of approximately 50×50 km² (depending somewhat on incidence angle), whereas the zeroth visibility reference antenna observes an area of approximately $\pi(1500^2)$ km². The observed strength of the RFI source will be higher in the spatial domain, relative to the visibility domain, by a factor of ~ 2800 ($= \pi * (1500)^2 / 50^2$). This factor can also be viewed as the ratio between the actual gain of the reference radiometer’s antenna and the gain of the effective antenna that is formed by Fourier synthesis.

RFI detectability in these two domains can also be understood in terms of the concept of sparsity. A sparse representation effectively means an efficient representation of a vector. For example, a single tone sinusoidal wave has a sparse representation in the frequency domain. In the frequency domain, only one principle component (its frequency) is needed to describe the signal, while the rest of the values are zero. In the time domain, all the time domain samples are required to fully describe the sinusoidal wave, and hence, it is not an efficient representation. A sparse representation is an efficient signal model [24], with only a few principle components required to describe the signal. As an illustration, Fig. 2 represents a sinusoidal wave added to Gaussian noise. While it is difficult to distinguish the noisy sinusoidal wave in the time domain, it is much easier to detect it in the frequency domain by the two clear peaks above the background noise floor.

The same principle applies with the SMOS visibility and spatial domains. Single point source RFI has a more sparse representation in the spatial domain relative to the visibility domain. A single principle component is required to describe a point source in the spatial domain, whereas in the visibility domain, all N visibility elements (or unique antenna pairs) are required to describe the same point source. The RFI signal power increases by a factor of N when going from the visibility domain to the spatial domain. For SMOS, the number of visibility elements is 2346 [25]. Similar to the previous results, RFI signal strength is ~ 2346 times stronger in the spatial domain.

Noise also increases when going from the visibility domain to the spatial domain. The visibility domain has an rms noise

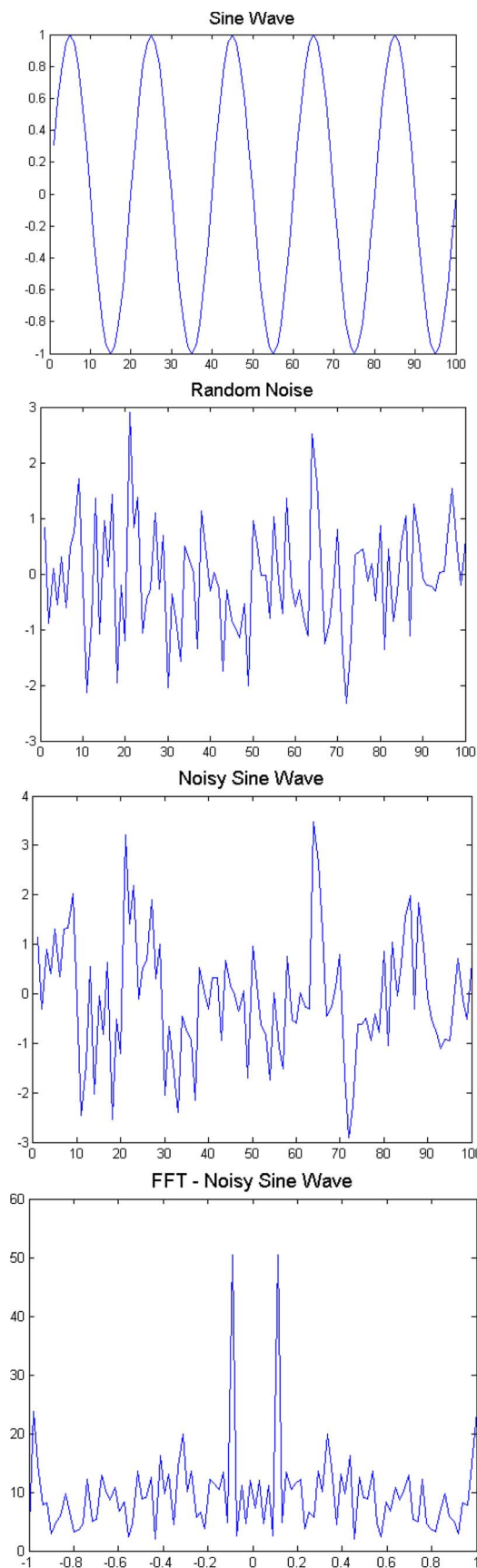


Fig. 2. Illustration of (a) sinusoidal wave in time domain, (b) Gaussian noise in time domain, (c) combined signals in time domain, representing an indistinguishable noisy sinusoidal wave, and (d) combined signals in frequency domain, with clear peaks distinguishable from the noise floor.

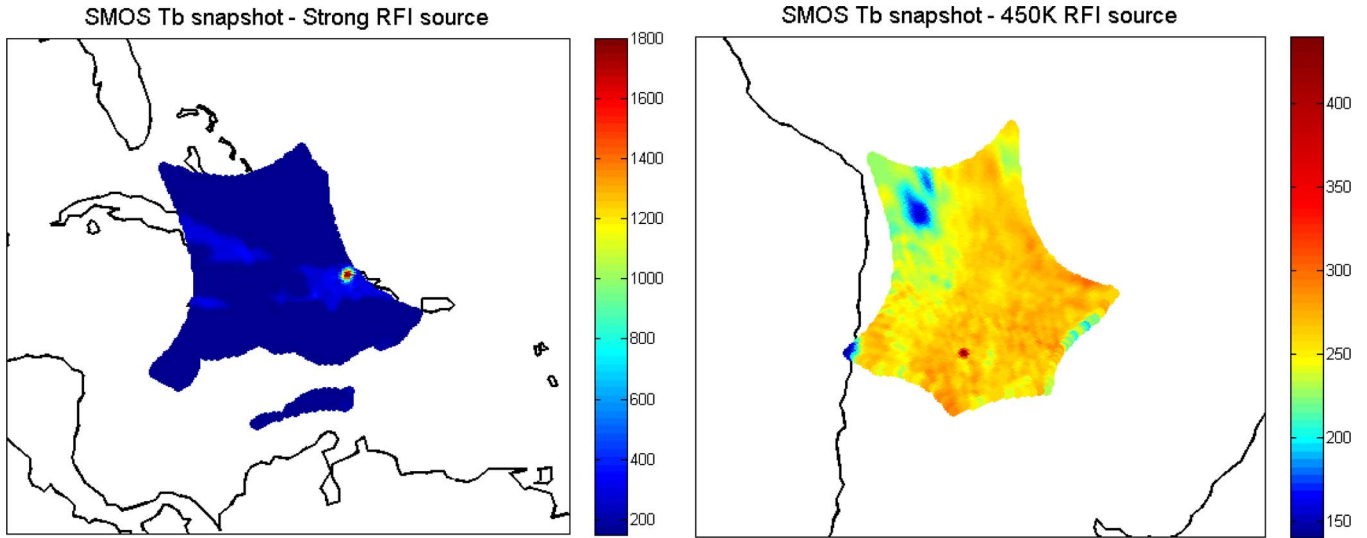


Fig. 3. Two SMOS snapshots contaminated by single point source RFIs. (a) RFI Tb = 1500 K. (b) RFI Tb = 150 K.

level of approximately 0.2 K. Noise increases by a factor of $N^{1/2}$ in the spatial domain due to error magnification by the image reconstruction algorithm. In terms of SMOS, this results in an NE Δ T of approximately 5 K ($= 0.2 \text{ K} * (2346)^{1/2}/2$). The factor of 2 in the denominator is due to the required double-sided RFI threshold in the Tb domain. Unlike the visibility domain, the positive definite L2-norm constraint on RFI perturbations is not possible in the spatial domain. Based on an increase by a factor of N in RFI signal strength and a factor of $N^{1/2}$ in noise level, the overall SNR of RFI increases by a factor of $N^{1/2}$ when going from the visibility to the spatial domain.

Applying a 3σ ($SNR = 3$) detection threshold, we note that the minimum detectable RFI strength in the visibility domain occurs if the zeroth visibility (V_o) is above 0.6 K. This corresponds to a point source Tb of 1380 K. The spatial domain can detect an RFI signal above 15 K in strength, which corresponds to V_o of 0.005 K.

Fig. 3 provides two RFI scenarios in which the algorithm performances of the two domains will differ. Fig. 3(a) shows a clear RFI spot of approximate signal strength of 1500 K (after removing thermal background). This RFI point source is equivalent to V_o of 0.65 K in the visibility domain, which is just above the detection threshold and would be detectable by both algorithms. Fig. 3(b) shows a clear RFI spot of around 150 K. This RFI spot is easily detectable in the spatial domain but amounts to only 0.065 K in the zeroth visibility, placing it well below the noise floor and undetectable.

It should be noted that, as the number of RFI point sources increases, the relative performance of the visibility domain algorithm improves, relative to the spatial domain, since all the sources will add together in the zeroth visibility measurements.

B. Angular Domain Versus Spatial Domain

Signal and noise considerations in the angular domain are the same as in the spatial domain since the angular domain operates

on Tb's obtained from different snapshot images. The SNR of RFI is the same in both domains. As a result, in terms of SNR, the angular domain algorithm comparison with a visibility domain-based algorithm is very similar to the spatial domain comparison discussed in the previous section. However, the angular domain presents an advantage over the spatial domain because of the smooth dependence of Tb on incidence angle and, hence, the ability to accurately estimate what the Tb of a sample under test should be from its neighboring samples. This permits a more accurate estimation of the expected value of the sample under test. The expected value is used to set the detection threshold for RFI. The detection threshold in both spatial and angular domains is given by the allowed deviation from the expected value of a sample under test. If the expected value is incorrectly predicted, then the threshold will be incorrectly set, which can result in false alarms or missed detections. In addition, in the case of the spatial domain, the allowed deviation of a sample under test from its expected value needs to be wider since spatial variations in Tb can be much larger without the presence of RFI due to the potential natural spatial variability of the scene.

The degree to which the expected value of a sample under test can be reliably estimated from its neighbors can be quantified by considering the autocorrelation of the samples. Examples are shown in Figs. 4 and 5 for samples in both the spatial and angular domains, derived empirically from a half orbit of SMOS observations.

In case of the angular domain, each sample is correlated to the next sample based on the geophysical relationship between Tb and incidence angles. Correlation between samples in the spatial domain is more or less random (e.g., forest land next to a lake), and any correlation is introduced by the antenna pattern of SMOS. Fig. 4 shows the correlation relationship between an angular domain sample and its neighbors. This relationship is derived from one half orbit of SMOS over land and one half orbit over water. The two colored curves in the figure explain the correlation between a sample at the edge fitted with the help of samples ahead of it and

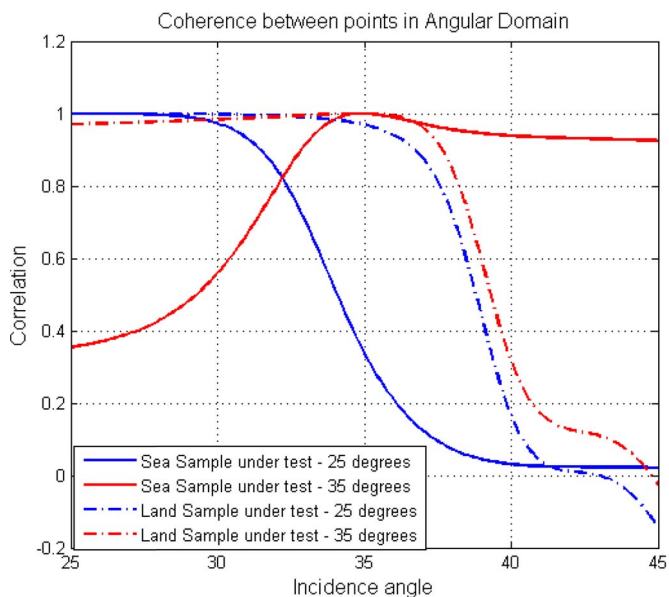


Fig. 4. Correlation statistics between an angular domain sample and its neighboring pixels based on two SMOS half orbits. The blue curve represents correlation between a sample under test at 25° incidence angle, and the red curve represents a sample under test at 35° incidence angle. The dashed line represents land statistics, and the solid line represents sea statistics.

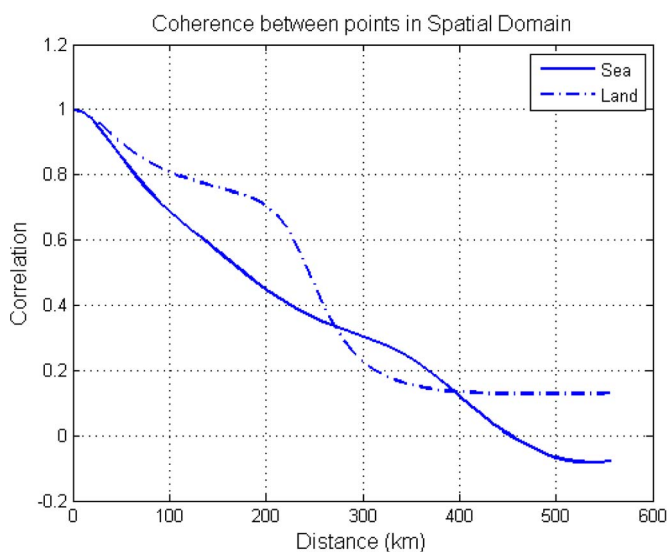


Fig. 5. Correlation statistics between a spatial domain sample and its neighboring pixels based on two SMOS half orbits. The dashed line represents land statistics, and the solid line represents sea statistics.

a sample in the middle fitted with correlated samples before and after it. In order to calculate autocorrelation statistics, a large population of Tb versus incidence angle measurements was used. These measurements were then fit with a cubic function to obtain Tb values at uniform incidence angles. The autocorrelation was then calculated from this large population of individual cubic fits based on their corresponding measurements.

Fig. 5 shows the correlation statistics in the spatial domain. Similar to Fig. 4, a large population set of Tb samples and their neighboring pixels were collected and quadratically fit. Auto-

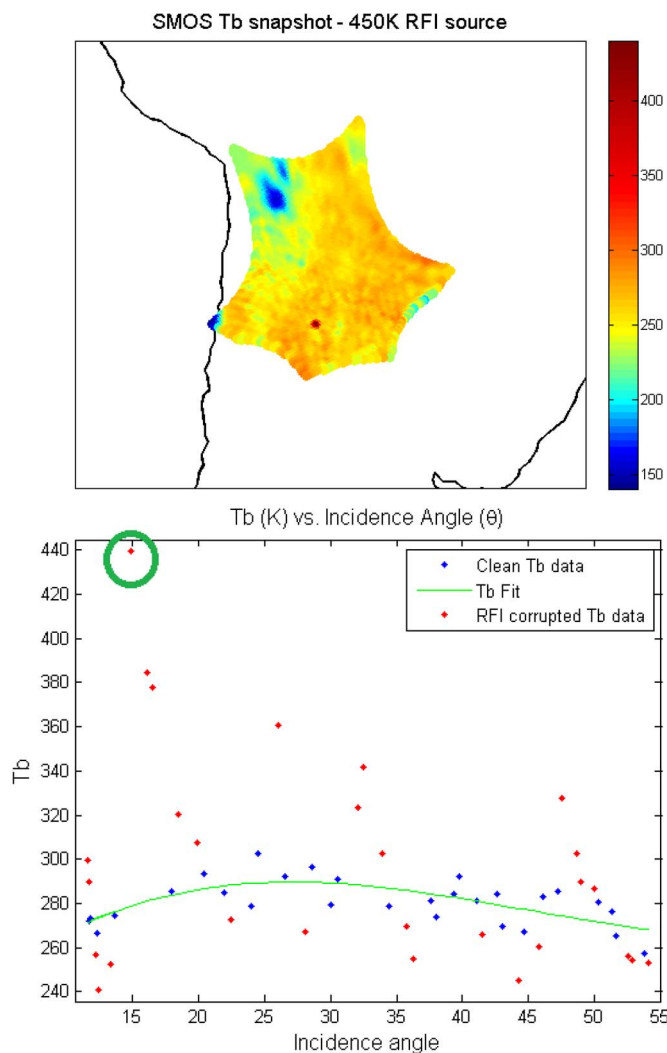


Fig. 6. (a) SMOS H-pol Tb snapshot with a clear RFI spot at 450 K (bright red). (b) Angular domain representation of the same RFI pixel with (red) flagged RFI Tbs, (blue) RFI-free Tbs, and (green) cubic fit. The circled sample in (b) is the same pixel as the red hot spot in (a).

correlation statistics are calculated from the population of fits obtained from observations. Fig. 5 shows less of a correlation in the spatial domain compared to the angular domain. As a result, coherence is worse in the spatial domain, leading to a noisier fit, noisier threshold, and higher false alarms and missed detections.

It should be noted that the spatial fit is performed by calculating the mean, i.e., zeroth order, which has lesser unexplained variance compared to a third-order fit performed in the angular domain.

IV. ANGULAR DOMAIN RESULTS

The performance of the angular domain RFI detection algorithm described in Section II-C1 is demonstrated by several representative examples of overpasses by SMOS of highly localized unphysically strong “hot spots” in the Tb image. These are likely caused by RFI sources, although precise ground truth assessment of this assumption is not readily available.

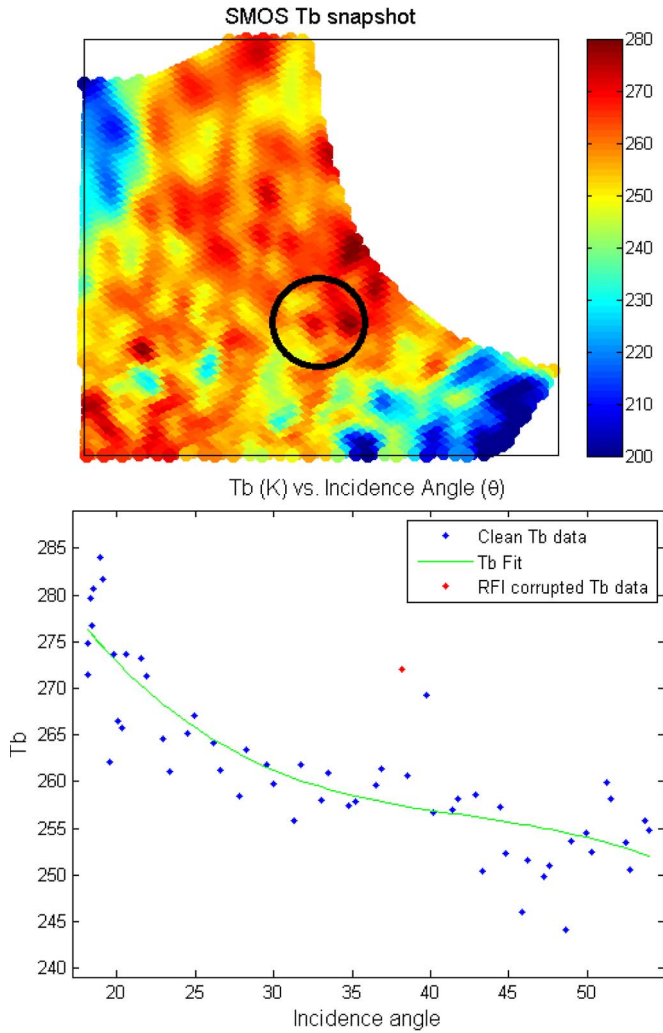


Fig. 7. (a) SMOS H-pol Tb snapshot with an indistinct RFI spot within the circle. (b) Angular domain representation of the same lake pixel with (red) flagged RFI Tb, (blue) RFI-free Tbs, and (green) cubic fit.

A. RFI Detection

Fig. 6(a) shows a SMOS snapshot of horizontally polarized (H-pol) Tb over South America which includes a clear RFI outlier of ~ 450 K. Fig. 6(b) shows samples at the location of the RFI point (RFI sample circled) when viewed in the angular domain. All samples colored red in Fig. 6(b) are flagged as RFI, all blue samples are assumed to be RFI free, and the green curve represents a fit. Note that both the low- and the high-level RFI are flagged by the algorithm.

Fig. 7 illustrates a key advantage of the angular domain detector. As observed in the circled region of the snapshot image [see Fig. 7(a)], an RFI source is indistinguishable from its neighboring pixels due to its low power and the high spatial variability of the natural emission. In the angular domain image [see Fig. 7(b)], on the other hand, an outlying RFI-corrupted sample is clearly evident, as indicated by the red dot. Fig. 7(b) also shows a neighboring incidence angle sample at 40° with similar characteristics to the flagged RFI sample. This sample is not flagged as RFI since it is below the algorithm detection threshold and is a possible example of a missed detection.

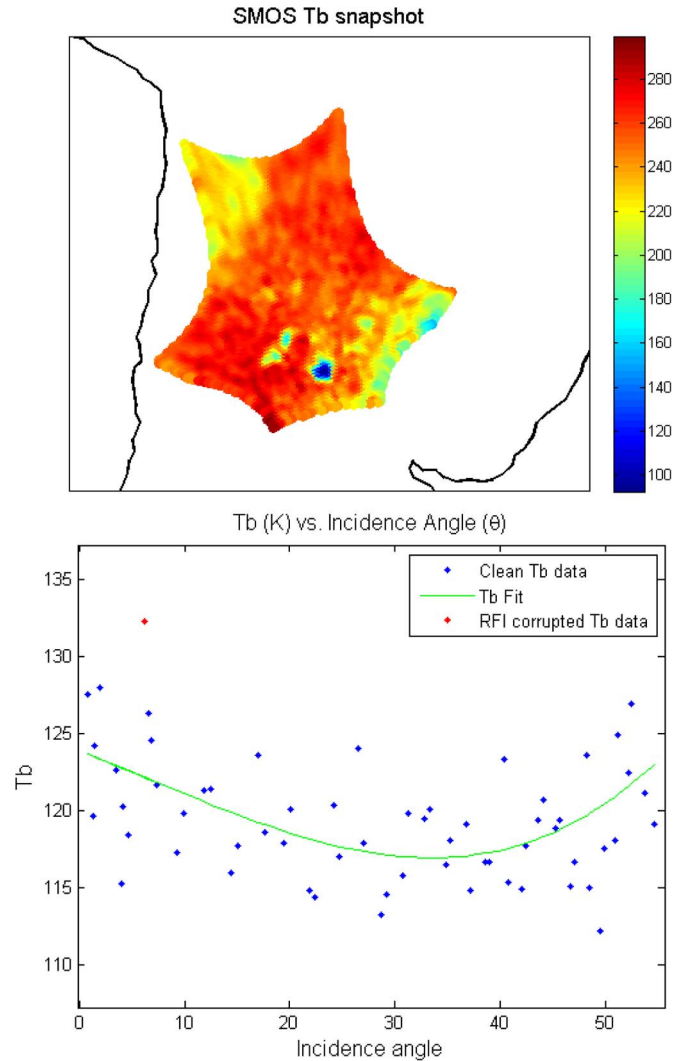


Fig. 8. (a) SMOS H-pol Tb snapshot with a low Tb lake surrounded by high Tb land. (b) Angular domain representation of the same lake pixel with (red) flagged RFI Tbs, (blue) RFI-free Tbs, and (green) cubic fit.

B. False-Alarm Sensitivity

The angular domain algorithm operates on a single grid point location and is not influenced by any of its neighboring pixels in the snapshot domain. This helps in avoiding false alarms such as the misinterpretation of an island surrounded by lower Tb water as RFI. Fig. 8 gives an example of a lake at cold Tbs surrounded by hotter land. Since RFI can be positively or negatively biased with SMOS, a pixel in the lake might also be falsely identified as RFI in the spatial domain algorithm. As can be seen in Fig. 8(b), most of the samples are identified as RFI free by the angular domain algorithm. One sample, near 10° incidence angle, is flagged as RFI contaminated. However, it is positively biased in a lake which is cooler than its neighboring pixels. Such an RFI pixel might be hard to detect in the spatial domain.

The FAR of the angular domain algorithm can be estimated by considering Tb samples to be a normally distributed random variable with a standard deviation of $NE\Delta T$. The expected Tb value of a sample under test (the value of the cubic fit at the incidence angle of the sample under test) can also be considered

to be a normally distributed random variable, with a standard deviation (σ_{mse}) given by the mean square error (mse) of the fit. The FAR then follows as

$$\begin{aligned}
 FAR &= E \left[\frac{1}{2} \left(1 - \operatorname{erf} \left(\frac{z-c}{\sqrt{2}} \right) \right) + \frac{1}{2} \left(1 - \operatorname{erf} \left(\frac{z+c}{\sqrt{2}} \right) \right) \right] \\
 &= 1 - \operatorname{erf} \left(\frac{z}{\sqrt{2(1+\sigma_{mse})}} \right)
 \end{aligned} \tag{4}$$

where $z = 3$ and $c \sim N(0, \sigma_{mse})$. Equation (4) suggests that the FAR will depend on the goodness of the cubic fit. If the fit is perfect (i.e., $\sigma_{mse} = 0$), then the FAR is identical to a normal Gaussian threshold detector. The FAR value calculated for each pixel flagged as RFI can be used as a confidence factor in the detection result. It should be noted though that the mse might be large due to the presence of a persistent RFI source (present in multiple incidence angle samples at the same location), thus impacting the cubic fit.

C. Negatively Biased RFI

The angular domain algorithm also detects and flags negatively biased RFI values. These Tb values are generally cooler than their surrounding spatial pixels or incidence angle measurements. As noted earlier, the reason for negatively biased Tb values is likely the Gibbs ringing, and the actual RFI source is probably not located at the pixel at which the negatively biased Tb is detected. This is hard to confirm with SMOS data due to multiple positively and negatively biased RFI sources present in any snapshot image.

As an example, the circled region in Fig. 9(a) shows an unusually cold Tb region next to a lake and a very bright RFI hot spot to its west. The angular domain plot in Fig. 9(b) shows the anomalous negatively biased RFI spot, which is clearly an outlier.

D. RFI Snapshot

The angular domain detection algorithm permits RFI to be detected at much lower levels than algorithms based in the spatial domain. With the angular domain algorithm, snapshot images can be generated of low-level RFI. Existing RFI algorithms in use by SMOS, which operate in the spatial domain [16], have generally indicated that the North American continent is relatively RFI free. While this may well be true for high-level RFI, it does not appear to be the case for low-level RFI. Fig. 10 shows one example of Tb snapshot over the eastern U.S., together with the corresponding RFI snapshot generated using the angular domain detection algorithm. Red pixels indicate possible RFI sources, and green represents RFI-free locations. Fig. 10 shows that the U.S. might not be as RFI free as previously believed. Note that the locations with RFI indicated in the RFI snapshot are not obviously contaminated (i.e., unnaturally bright) in the Tb snapshot image.

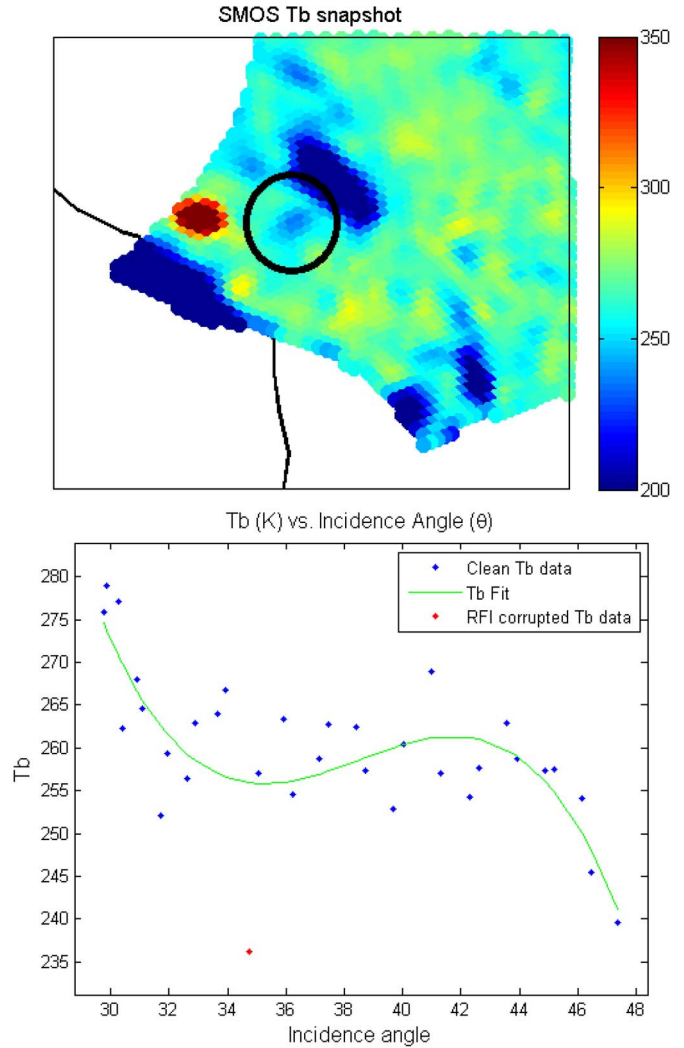


Fig. 9. (a) SMOS H-pol Tb snapshot with a negatively biased RFI region (circle). (b) Angular domain representation of one of the pixels in cold RFI region with (red) flagged RFI Tbs, (blue) RFI-free Tbs, and (green) cubic fit.

E. Algorithm Performance

In general, the absence of reliable RFI “ground truth” makes it very difficult to quantitatively assess the detectability statistics of an RFI algorithm. Comparisons of histograms of Tb samples containing flagged and unflagged samples give some information about the behavior of the algorithm. Fig. 11 shows Tb histograms accumulated over a single half orbit. The blue curve is derived from all of the Tb data; the green curve is derived only from Tb data classified as RFI free. The two curves have generally similar shapes since a large percentage of data are RFI free. The bimodal distribution of the histogram is a result of the large TB difference between land and water.

The red curve indicates Tb data classified as containing RFI by the angular domain detection algorithm. Two things are noteworthy: 1) The algorithm immediately discards extremely high or extremely low outlier Tb samples since the algorithm uses a hard threshold for initial detection, and 2) most of the RFI detected between 50 K and 300 K has similar characteristics to the clean Tb data with slight variations. The red histogram peak around 100 K is slightly offset toward higher values with respect to the blue and green curves, also noted by the lower

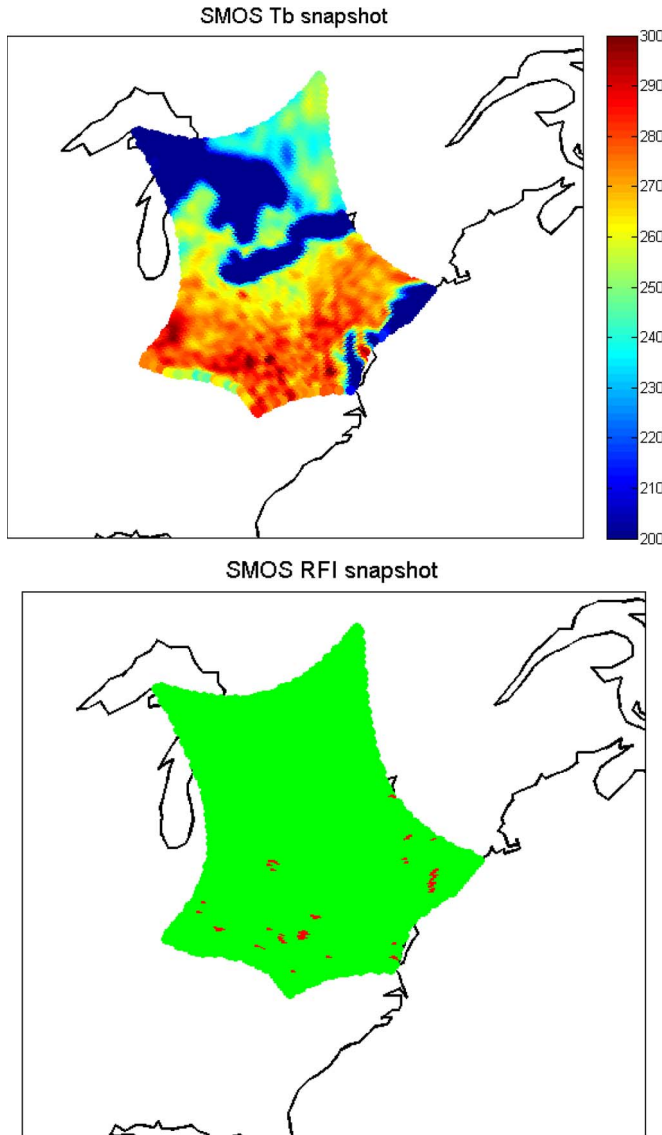


Fig. 10. (a) SMOS H-pol Tb snapshot over the eastern U.S. at 10:50:36 Coordinated Universal Time (UTC) on July 8, 2010. (b) SMOS RFI snapshot at the same time over eastern U.S. (red = RFI present and green = RFI free).

dip of the green curve with respect to the blue curve around the valley near 150 K. Also, between 200 K and 300 K, the RFI flagged data do not exhibit a similar valley around 250 K as observed with the blue and green curves. This suggests that the algorithm is able to detect low-level RFI-corrupted samples that are very close to the natural scene. Some of the flagged RFI samples in both cases are false alarms described by (4).

V. SUMMARY AND DISCUSSION

The interferometric nature of SMOS allows for RFI detection algorithms to operate in a number of signal domains. RFI detection can be applied in the early L1a data processing stage, in the visibility domain, where temporal samples of zeroth visibility are monitored for outliers. Converting to spatial Tbs from visibilities allows for the detection of RFI “hot spots” by comparing a pixel with its neighboring (in space) pixels. A third detection domain is available because SMOS measures the Tb at a single location over multiple incidence angles. Tb has a

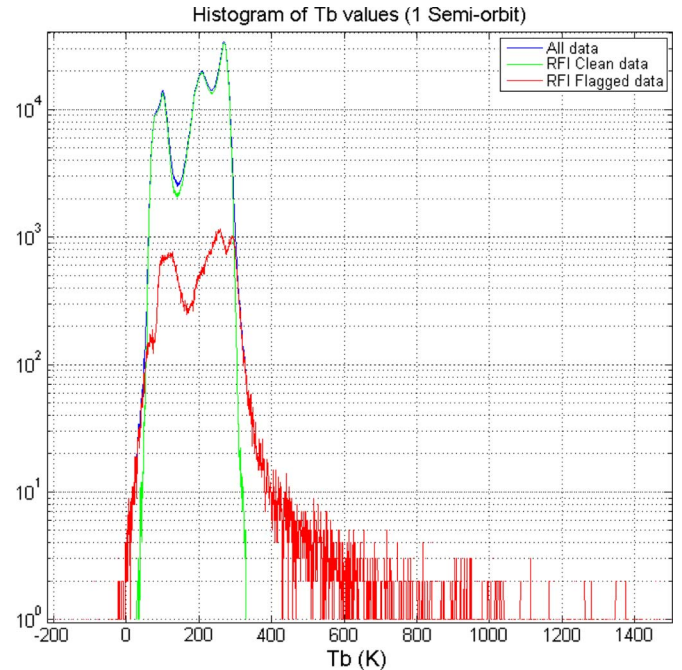


Fig. 11. Histogram of Tb values over a single half orbit, sweeping from the south to the north pole between 17° W and 95° W approximately, measured on July 8, 2010, from 10:10 to 11:05 UTC. (Blue = All Tb data, Green = RFI free Tb data, and Red = RFI corrupted Tb data).

specific geophysical relationship with incidence angle, and an angular domain RFI detection algorithm has been implemented which checks for deviations of the Tbs from the expected Tb–incidence angle variations.

The noise level of Tbs increases by a factor of approximately 25 (from 0.2 K to 5 K) when going from the visibility to the spatial domain. The power of a single-point RFI source, on the other hand, is enhanced by a factor of ~ 2300 when going from the visibility to the spatial domain. Thus, it is easier to detect RFI in the spatial domain due to a higher RFI SNR. The angular domain has the same SNR as the spatial domain. The angular domain algorithm has an advantage over the spatial domain algorithm in that there is a more deterministic relationship between a sample under test and its neighbors in the angular domain. This relationship allows a more accurate prediction of the expected value of a sample under test from its neighbors, thus aiding in detection and false-alarm statistics.

The algorithm identifies positively biased as well as negatively biased RFI points. Low-level (near $NE\Delta T$) RFI is more easily detected. RFI snapshots, made by applying the angular domain algorithm to regional SMOS images, indicate RFI at locations previously considered to be relatively RFI free. Histogram comparisons of Tb data flagged and unflagged for RFI suggest that, aside from some strong outlier (high and low) Tb values, most of the RFI flagged is low level.

The RFI detection algorithm discussed in this paper can also be used as a means for mitigating corrupt RFI samples. The average from multiple Tb fits with respect to incidence angle can be used to mitigate RFI at a particular sample. The accuracy of the fit can be calculated using a root sum square metric of the fit mses. Future work will involve investigating the validity of such a mitigation approach.

ACKNOWLEDGMENT

The authors would like to thank the anonymous reviewers for their useful comments.

REFERENCES

- [1] Y. H. Kerr, P. Waldteufel, J. P. Wigneron, S. Delwart, F. Cabot, J. Boutin, M. J. Escorihuela, J. Font, N. Reul, C. Gruhier, S. E. Juglea, M. R. Drinkwater, A. Hahne, M. Martin-Neira, and S. Mecklenburg, "The SMOS mission: New tool for monitoring key elements of the global water cycle," *Proc. IEEE*, vol. 98, no. 5, pp. 666–687, May 2010.
- [2] Y. H. Kerr, P. Waldteufel, J. P. Wigneron, J. Martinuzzi, J. Font, and M. Berger, "Soil moisture retrieval from space: The Soil Moisture and Ocean Salinity (SMOS) mission," *IEEE Trans. Geosci. Remote Sens.*, vol. 39, no. 8, pp. 1729–1735, Aug. 2001.
- [3] D. M. Le Vine, "ESTAR experience with RFI at L-band and implications for future passive microwave remote sensing from space," in *Proc. IEEE IGARSS*, 2002, vol. 2, pp. 847–849.
- [4] S. Misra, S. S. Kristensen, S. S. Sobjaerg, and N. Skou, "CoSMOS: Performance of kurtosis algorithm for radio frequency interference detection and mitigation," in *Proc. IEEE IGARSS*, 2007, pp. 2714–2717.
- [5] N. Skou, S. Misra, J. E. Balling, S. S. Kristensen, and S. S. Sobjaerg, "L-band RFI as experienced during airborne campaigns in preparation for SMOS," *IEEE Trans. Geosci. Remote Sens.*, vol. 48, no. 3, pp. 1398–1407, Mar. 2010.
- [6] P. O'Neill, M. Owe, B. Gouweleuw, E. G. Njoku, J. C. Shi, and E. Wood, "Hydros soil moisture retrieval algorithms: Status and relevance to future mission," in *Proc. IEEE IGARSS*, 2006, pp. 436–439.
- [7] B. Guner, J. T. Johnson, and N. Niamsuwan, "Time and frequency blanking for radio-frequency interference mitigation in microwave radiometry," *IEEE Trans. Geosci. Remote Sens.*, vol. 45, no. 11, pp. 3672–3679, Nov. 2007.
- [8] J. T. Johnson, G. A. Hampson, and S. W. Ellingson, "Design and demonstration of an interference suppressing microwave radiometer," in *Proc. IEEE IGARSS*, 2004, vol. 3, pp. 1683–1686.
- [9] S. Misra and C. S. Ruf, "Detection of radio-frequency interference for the Aquarius radiometer," *IEEE Trans. Geosci. Remote Sens.*, vol. 46, no. 10, pp. 3123–3128, Oct. 2008.
- [10] B. Guner, N. Niamsuwan, and J. T. Johnson, "Performance study of a cross-frequency detection algorithm for pulsed sinusoidal RFI in microwave radiometry," *IEEE Trans. Geosci. Remote Sens.*, vol. 48, no. 7, pp. 2899–2908, Jul. 2010.
- [11] A. J. Gasiewski, M. Klein, A. Yevgrafov, and V. Leuskiy, "Interference mitigation in passive microwave radiometry," in *Proc. IEEE IGARSS*, 2002, vol. 3, pp. 1682–1684.
- [12] C. S. Ruf, S. M. Gross, and S. Misra, "RFI detection and mitigation for microwave radiometry with an agile digital detector," *IEEE Trans. Geosci. Remote Sens.*, vol. 44, no. 3, pp. 694–706, Mar. 2006.
- [13] S. Misra, P. N. Mohammed, B. Guner, C. S. Ruf, J. R. Piepmeier, and J. T. Johnson, "Microwave radiometer radio-frequency interference detection algorithms: A comparative study," *IEEE Trans. Geosci. Remote Sens.*, vol. 47, no. 11, pp. 3742–3754, Nov. 2009.
- [14] J. M. Tarongi and A. Camps, "Normality analysis for RFI detection in microwave radiometry," *Remote Sens.*, vol. 2, no. 1, pp. 191–210, Jan. 2010.
- [15] J. E. Balling, S. S. Sobjaerg, S. S. Kristensen, and N. Skou, "RFI and SMOS: Preparatory campaigns and first observations from space," in *Proc. 11th Spec. Meeting Microw. Radiometry Remote Sens. Environ.*, 2010, pp. 282–287.
- [16] A. Camps, J. Gourrion, J. M. Tarongi, A. Gutierrez, J. Barbosa, and R. Castro, "RFI analysis in SMOS imagery," in *Proc. IEEE IGARSS*, 2010, pp. 2007–2010.
- [17] H. M. J. Barre, B. Duesmann, and Y. H. Kerr, "SMOS: The mission and the system," *IEEE Trans. Geosci. Remote Sens.*, vol. 46, no. 3, pp. 587–593, Mar. 2008.
- [18] E. Anterrieu, "On the detection and quantification of RFI in L1a signals provided by SMOS," *IEEE Trans. Geosci. Remote Sens.*, vol. 49, no. 10, pp. 3986–3992, Oct. 2011.
- [19] ESA, SMOS Calibration Validation and Retrieval Plan, Apr. 2010.
- [20] A. Camps, I. Corbella, M. Vall-Ilossera, N. Duffo, F. Marcos, F. Martinez-Fadrique, and M. Greiner, "The SMOS end-to-end performance simulator: Description and scientific applications," in *Proc. IEEE IGARSS*, 2003, vol. 1, pp. 13–15.
- [21] L. Li, E. G. Njoku, E. Im, P. S. Chang, and K. S. Germain, "A preliminary survey of radio-frequency interference over the U.S. in Aqua AMSR-E data," *IEEE Trans. Geosci. Remote Sens.*, vol. 42, no. 2, pp. 380–390, Feb. 2004.
- [22] N. Skou, J. E. Balling, S. S. Sobjaerg, and S. S. Kristensen, "Surveys and analysis of RFI in the SMOS context," in *Proc. IEEE IGARSS*, 2010, pp. 2011–2014.
- [23] H. T. Friis, "A note on a simple transmission formula," *Proc. IRE*, vol. 34, no. 5, pp. 254–256, May 1946.
- [24] K. Huang and S. Aviyente, "Sparse representation for signal classification," in *Proc. Adv. Neural Inf. Process. Syst.*, 2006, pp. 609–616.
- [25] M. A. Brown, F. Torres, I. Corbella, and A. Colliander, "SMOS calibration," *IEEE Trans. Geosci. Remote Sens.*, vol. 46, no. 3, pp. 646–658, Mar. 2008.
- [26] E. Anterrieu and A. Khazaal, "Brightness temperature maps reconstruction from dual-polarimetric visibilities in synthetic aperture imaging radiometry," *IEEE Trans. Geosci. Remote Sens.*, vol. 46, no. 3, pp. 606–612, Mar. 2008.



Sidharth Misra (S'06–M'11) received the B.E. degree in electronics and communication engineering from the Nirma Institute of Technology, Gujarat University, Ahmedabad, India, in 2004, and the M.S. degree in electrical engineering and computer science—signal processing from the University of Michigan, Ann Arbor, in 2006, where he received the Ph.D. degree in the Department of Atmospheric, Oceanic and Space Sciences in 2011.

He is currently working in the Microwave Systems Technology group at the Jet Propulsion Laboratory, Pasadena, CA. He was a Research Engineer with the Space Physics Research Laboratory, University of Michigan, where he worked on the analysis and implementation of the agile digital receiver for radio-frequency interference (RFI) mitigation. He was a Research Assistant with the Danish National Space Center, Technical University of Denmark (DTU), Lyngby, Denmark. He was also with the Space Applications Center, Indian Space Research Organization, Ahmedabad. He has many publications in the field of RFI detection and mitigation. He is currently working on the Aquarius radiometer calibration, as well as the TOPEX geophysical data record (GDR) reprocessing. His research interests involve microwave radiometry, signal detection and estimation, and coastal altimetry.

Dr. Misra was the recipient of the International Geoscience and Remote Sensing Symposium (IGARSS) 2006 Symposium Prize Paper Award and the Mikio Takagi award at the IGARSS 2009 student prize paper competition.



Christopher S. Ruf (S'85–M'87–SM'92–F'01) received the B.A. degree in physics from Reed College, Portland, OR, and the Ph.D. degree in electrical and computer engineering from the University of Massachusetts, Amherst.

He is currently a Professor of atmospheric, oceanic, and space sciences; a Professor of electrical engineering and computer science; and the Director of the Space Physics Research Laboratory with the University of Michigan, Ann Arbor. He has worked previously at Intel Corporation, Hughes Space and Communication, the National Aeronautics and Space Administration (NASA) Jet Propulsion Laboratory, Pasadena, CA, and Penn State University, University Park. In 2000, he was a Guest Professor with the Technical University of Denmark (DTU), Lyngby, Denmark. He has published in the areas of microwave radiometer satellite calibration, sensor and technology development, and atmospheric, oceanic, land surface, and cryosphere geophysical retrieval algorithms.

Dr. Ruf is a member of the American Geophysical Union (AGU), the American Meteorological Society (AMS), and Commission F of the Union Radio Scientifique Internationale. He has served on the editorial boards of the *AGU Radio Science*, the *IEEE TRANSACTIONS ON GEOSCIENCE AND REMOTE SENSING* (TGRS), and the *AMS Journal of Atmospheric and Oceanic Technology*. He is currently the Editor-in-Chief of TGRS. He has been the recipient of three NASA Certificates of Recognition and four NASA Group Achievement Awards, as well as the 1997 TGRS Prize Paper Award, the 1999 IEEE Resnik Technical Field Award, and the 2006 International Geoscience and Remote Sensing Symposium Prize Paper Award.